SAND2017-4645C

Pulse-Burst PIV of the Supersonic Wake of a Wall-Mounted Hemisphere

Steven J. Beresh,[1] John F. Henfling,[2] and Russell W. Spillers[3]
Sandia National Laboratories, Albuquerque, NM, 87185

Time-resolved particle image velocimetry (PIV) was conducted at 40 kHz using a pulse-burst laser in the supersonic wake of a wall-mounted hemisphere. Velocity fields suggest a recirculation region with two lobes in which flow moves away from the wall near centerline and recirculates back towards the hemisphere off centerline. Spatio-temporal cross-correlations and conditional ensemble averages relate the characteristic behavior of the unsteady shock motion to the flapping of the shear layer. At Mach 1.5, oblique shocks form associated with vortical structures in the shear layer and convect downstream in tandem; a weak periodicity is observed. Shock motion at Mach 2.0 is somewhat different, wherein multiple weak disturbances propagate from shear layer turbulent structures to form an oblique shock that ripples as these vortices pass by. Bifurcated shock feet coalesce and break apart without evident periodicity. Power spectra show a preferred frequency of shear layer flapping and shock motion at 5.6 kHz for Mach 1.5, but at Mach 2.0 a weak preferred frequency of 6.7 kHz is found only for the oblique shock motion and not the shear layer unsteadiness.

Introduction

Many aircraft employ protuberances or blisters based on hemispherical geometries to house optical sensors, laser beams, electronics pods, or airborne telescopes. Motivated by these applications, the flow over transonic turrets has been the subject of a number of studies, with primary attention paid to the separated region [1]. A number of recent experiments have examined the unsteady motion of the shock that forms near the upper surface of a hemisphere. Reid et al [2] and Fang et al [3] noted the unsteadiness of the shock over a hemisphere under transonic conditions, and Morrida et al [4, 5] tracked the shock motion over long time periods. Combined with their earlier measurements for the related geometry of a hemisphere capping a cylinder [6] and those by Goorskey et al [7] and De Lucca et al [8], these experiments found broadband frequency content to the shock motion rather than any oscillatory behavior, consistent with a canonical shock/boundary layer interaction. Beresh et al [9] correlated the shock motion to the turbulent separation region in the wake of the hemisphere and concluded that the dominant mechanism for the shock motion is the instability found in the separated flow.

Conversely, no published experiments have studied the turbulent wake of a hemisphere in supersonic flow, although Coirier et al [10] and Morgan et al [11] have computationally simulated such a flow. Gordeyev and Jumper's review [1] suggests that the separated wake will become smaller at supersonic speeds, but they admit this is largely conjectural as no known data are available to confirm the wake structure. As computations begin to explore this regime, data are needed to establish whether the wake of a hemisphere differs in supersonic flow from the more widely explored subsonic or transonic flow regimes. Moreover, studies of the dynamics of the hemisphere wake would be valuable to ensure that simulations can adequately reproduce the unsteadiness of the flow.

Meanwhile, the measurement capability of time-resolved particle image velocimetry (TR-PIV) has evolved as a

[1]Distinguished Member of the Technical Staff, Engineering Sciences Center, AIAA Associate Fellow, correspondence to: P.O. Box 5800, Mailstop 0825, (505) 844-4618, email: sjberes@sandia.gov
[2]Distinguished Technologist
[3]Principal Technologist

means of measuring temporally correlated velocity fields, allowing the acquisition of PIV movies. In high-speed flows, TR-PIV is best accomplished using a pulse-burst laser, as this is the only light source capable of producing sufficient energy at the necessarily rapid pulse rates, though with the penalty of a very low duty cycle. Simultaneous with the maturation of pulse-burst laser technology, quality high-speed cameras have begun to achieve desirable framing rates without excessive sacrifice of the size of the spatial array. Coupling these two technologies now permits application of TR-PIV in a production testing facility as demonstrated by Beresh et al in a transonic wind tunnel [12].

Experiments designed to advance studies of the turbulent wake of a hemisphere from transonic to supersonic speeds can profit from the use of pulse-burst PIV. Even the usual contributions of conventional PIV towards mean flow structure and turbulent stress fields would provide previously unavailable measurements concerning the wake of a hemisphere under supersonic conditions. Pulse-burst PIV additionally can measure the dynamics of this flow to establish the frequency content of the wake and the nature of its unsteady motion. These measurements therefore can offer previously unattainable insight into the physical behavior of the supersonic wake of a wall-mounted hemisphere at Mach 1.5 and 2.0.

Experimental Apparatus

Wind Tunnel and Hemisphere Model

Experiments were conducted in Sandia's Trisonic Wind Tunnel (TWT) at Mach 1.5 and 2.0. The TWT is a blowdown-to-atmosphere facility using air as the test gas through a test section of nominally 305 × 305 mm^2 (12 × 12 inch^2) enclosed in a pressurized plenum. In its supersonic configuration, the TWT's Mach numbers are varied by exchanging the top and bottom walls of the planar nozzle; Mach numbers 1.5, 2.0, 2.5, and 3.0 are available. Experiments were conducted in the TWT's half-nozzle test section, in which the top wall of each supersonic nozzle is retained and a single bottom wall replaces the lower supersonic nozzle wall. The new lower wall extends the inlet contour of the tunnel and then fairs into a flat surface at what previously would have been the test section centerline. This provides a flat plate working surface with convenient optical access within the "test rhombus" in which the supersonic expansion is complete. The resulting half-nozzle test section is 152 mm (6 inch) high and 305 mm (12 inch) wide. The half-nozzle configuration has been calibrated at each Mach number using wall pressure taps and Pitot surveys of the boundary layer, showing flow conditions to be sufficiently uniform and the wall boundary layer developing under equilibrium conditions at the testing location.

The TWT was operated at a stagnation pressure of 340 kPa for Mach 1.5 and 410 kPa for Mach 2.0. The wind tunnel stagnation temperature T_0 is fixed at 321K ± 2K by heating in the storage tanks, and the wall temperature is effectively constant at ambient conditions, T_w=307K ± 3K, though T_w tends to drift upward within this range as the wall warms during the course of a day. Pitot probe surveys have measured the 99%-velocity incoming boundary layer thickness as 12.4 mm and 10.5 mm at the two respective Mach numbers, to within an estimated uncertainty of ±0.15 mm. Freestream velocities U_∞ were measured from previous PIV experiments as 450 m/s and 535 m/s, respectively.

The hemisphere had a radius (and hence height) of 25.4 mm and was mounted on the top wall of the wind tunnel as seen in the photograph of Fig. 1a. It was fabricated from polished acrylic to minimize the flare of the laser sheet striking it and allow measurements near the hemisphere surface. The wall upon which it mounted contained a window along the centerline downstream of the hemisphere to minimize laser flare along this surface as well. Since laser light entering the transparent hemisphere created an intense glow due to internal reflection, which created blooming on the PIV cameras, the hemisphere was painted black except along a centerline strip where the laser sheet impinged upon it.

Pulse-Burst PIV System

The TWT is seeded by a thermal smoke generator (Corona Vi-Count 5000) that produces a large quantity of particles typically 0.2 - 0.3 μm in diameter from a mineral oil base. Particles are delivered to the TWT's stagnation chamber upstream of the flow conditioning section through a series of pipes and tubes, in which agglomeration of the particles occurs. Previous measurement of the *in-situ* particle response across a shock wave generated by a wedge showed the particle size to be 0.7 - 0.8 μm.

In the current work, a quasi-continuous burst-mode laser (QuasiModo-1000, Spectral Energies, LLC) with both diode- and flashlamp-pumped Nd:YAG amplifiers was used to produce a high-energy pulse train at 532 nm. The pulse-burst laser generates up to 10.2 ms duration bursts every 8 seconds with a maximum 532 nm pulse energy of 500 mJ at 5 kHz and 20 mJ pulse energy at its maximum repetition rate of 500 kHz. The laser is capable of producing doublets with variable interpulse spacing at all repetition rates, though in the present work the time between pulses in a doublet was 2.10 μs at Mach 1.5 and 1.80 μs at Mach 2.0. In each case, 40 kHz doublets were used for PIV measurements with energy per pulse of about 20 mJ at 532 nm for a 10.2 ms burst duration.

The laser sheet could be passed into the test section only from below and from a window far downstream after the

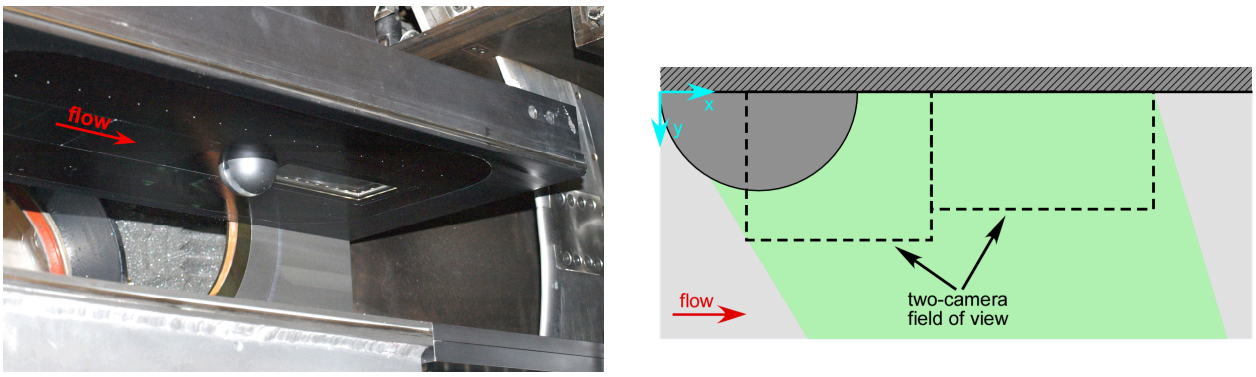

(a) (b)

Fig. 1: (a) Photograph of the hemisphere installed into the half-nozzle supersonic test section of the Trisonic Wind Tunnel. (b) Laser sheet and field of view for imaging.

nozzle curvature terminates. This necessitated an awkward beam path in which the laser sheet approached the hemisphere from downstream and could illuminate only the hemisphere wake up to slightly forward of its apex, as sketched in Fig. 1b.

Images were acquired using two high-speed CMOS cameras (Photron SA-Z) which have a full framing rate of 20 kHz and an array of 1024 × 1024 pixels at this speed. Their windowing function allows the framing rate to be increased by sampling a semi-arbitrary portion of the imaging array. In the present case, each camera operated at 80 kHz with the two pulses in a doublet frame-straddled around the cameras' interframe transfer time, which allowed cross-correlation analysis of pairs of images to produce PIV velocity fields at 40 kHz. The cameras each were equipped with 200-mm focal length lenses.

The two cameras were placed side by side to extend the field of view in the streamwise direction, with each camera independently acquiring two-component PIV measurements. Each camera was not set to image the same aspect ratio. One camera was positioned to image the near wake with a resolution of 512 × 424 pixels and the second camera imaged farther downstream in the wake at a resolution of 640 × 360 pixels. Both configurations are compatible with a 80 kHz framing rate. The differing aspect ratio was selected to account for the flow over the hemisphere surface and the subsequent narrowing of the wake. This yielded a combined field of view reaching approximately 75 mm downstream of the trailing edge of the hemisphere. Unfortunately, the large size of the camera bodies precluded placing them sufficiently close to one another to image the laser sheet from a normal direction. Therefore, they were canted at an angle of 3 deg such that their individual imaging regions were adjacent and could be combined for vector processing. This angle created a perspective bias on the velocity vectors due to added sensitivity to the out-of-plane velocity component, but calculations estimated that the maximum induced error is no more than 2%. This was considered to be an acceptable compromise in order to create the desired field of view. The combined field of view is shown in Fig. 1b along with the laser sheet projection; the origin of the coordinate axes was fixed to the leading edge of the hemisphere at the wind tunnel wall.

Data were processed using LaVision's DaVis v8.2. In each case, image pairs were background-corrected, intensity normalized, and then interrogated with an initial pass using 64 × 64 pixel interrogation windows, followed by two iterations of 24 × 24 pixel interrogation windows. A 50% overlap in the interrogation windows was used as well. The resulting vector fields were validated based upon signal-to-noise ratio, nearest-neighbor comparisons, and allowable velocity range. A single pass of light vector smoothing was employed as well. Mach 1.5 data have been constructed from 51 bursts and Mach 2.0 data from 26 bursts.

Particle Seeding Quality

The supersonic wake of a hemisphere is a very difficult flow to seed, for two reasons. First, the thin shear layer emanating from the separation point possesses strong velocity gradients that are difficult for particles to faithfully track. Second, the gas density immediately behind the hemisphere falls to low values and resists entrainment of particles.

To address the particle response, *in situ* measurements of the particle relaxation across a shock wave generated by a wedge have shown a response time of 1 – 2 μs, corresponding to an estimated diameter of 0.7 – 0.8 μm. The velocity gradients in the present flow were determined based on *a posteriori* analysis of the instantaneous PIV measurements,

then used to determine a Stokes number. The largest velocity gradients in the shear layer at Mach 1.5 yield a worst-case Stokes number of about 0.4; the corresponding value at Mach 2.0 is about 0.3, owing principally to smaller velocity gradients. These estimates are somewhat larger than desirable and suggest that some particle lag error may be present with a worst-case error of perhaps 3% [13, 14]. However, this would occur only for the very largest instantaneous velocity gradients due to turbulent fluctuations and the overall statistics accumulated for the flow would possess considerably smaller error. Maximum Stokes numbers in the recirculation region are about 1/3 of those in the shear layer owing to the weaker velocity gradients, with a correspondingly smaller potential for error.

The second seeding difficulty due to low density in the hemisphere wake proved to be more troublesome. At Mach 1.5, fewer particles were found in the immediate wake than in the shear layer or farther downstream, but rarely did this lead to invalid vectors. This was not the case at Mach 2.0. Here, loss of particles could be so extreme that the much of the wake was unmeasurable for a succession of frames within a burst sequence. This necessitated that numerous bursts at Mach 2.0 were discarded.

Figure 2 illustrates the problem by displaying the average intensity of the seeding density with overlaid contours of the valid vector rate. Figure 2a shows a typical burst at Mach 1.5 whereas Fig. 2b shows one of the poorer bursts at Mach 2.0 that nonetheless is considered acceptable. Although the seeding density at Mach 1.5 clearly is low in the near wake of the hemisphere, the valid vector rate exceeds 0.99 nearly everywhere. Most of the lower valid vector rates are concentrated near the seam between the two concatenated fields of view, reflecting increased particle dropout at the image boundary. Conversely, the seed density is even dimmer in the Mach 2.0 wake and remains so farther downstream. The valid vector rate falls to the range of 0.9 to 0.95 in this case, with again a greater concentration near the image seam. Rejected bursts were even poorer and showed elevated uncertainty even in vectors that passed the validation criteria.

Approximately half of the Mach 2.0 bursts were rejected due to inadequate seeding. Clearly, this presents a possibility of a selection bias if absent vectors are more likely to correspond to low-density turbulent events. To establish whether this may be the case, the 26 bursts that were retained were separated into two classes, one in which seeding was consistently strong (12 bursts) and another in which invalid vectors were more common (14 bursts).

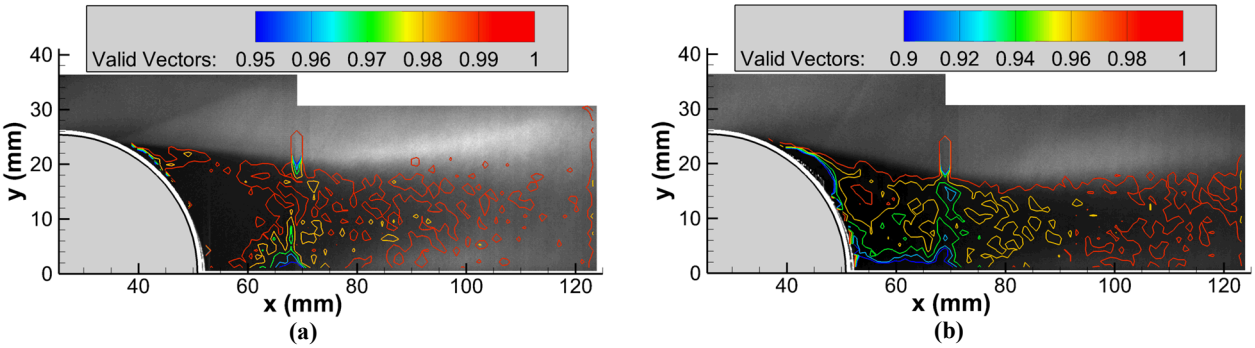

Fig. 2: Average particle seeding density with overlaid contours of the valid vector rate. (a) Mach 1.5; (b) Mach 2.0.

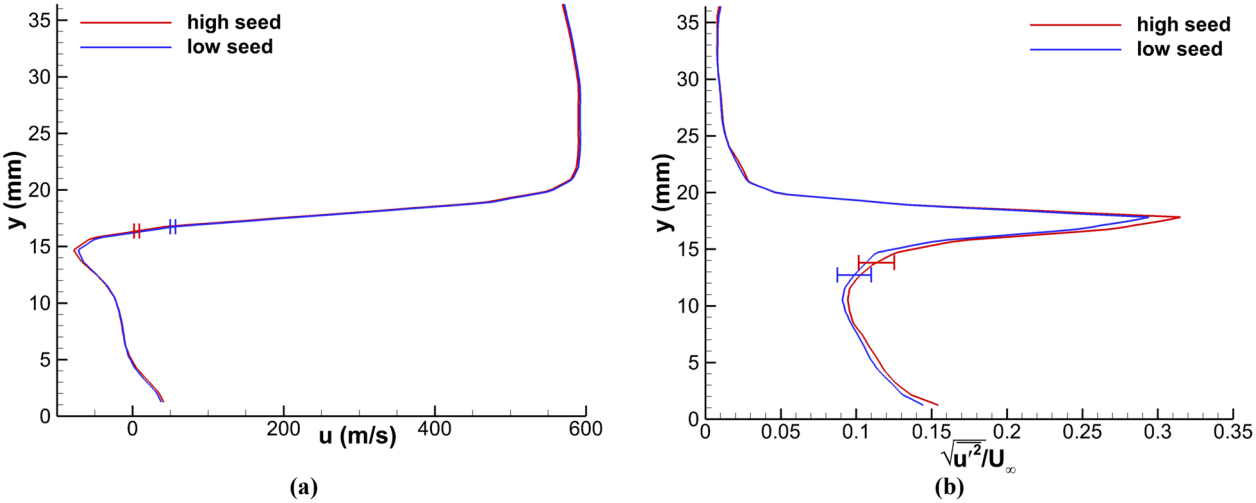

Fig. 3: Comparison of data acquired using high and low seeding densities at Mach 2.0 and x=60 mm. (a) mean streamwise velocity; (b) streamwise turbulent stress.

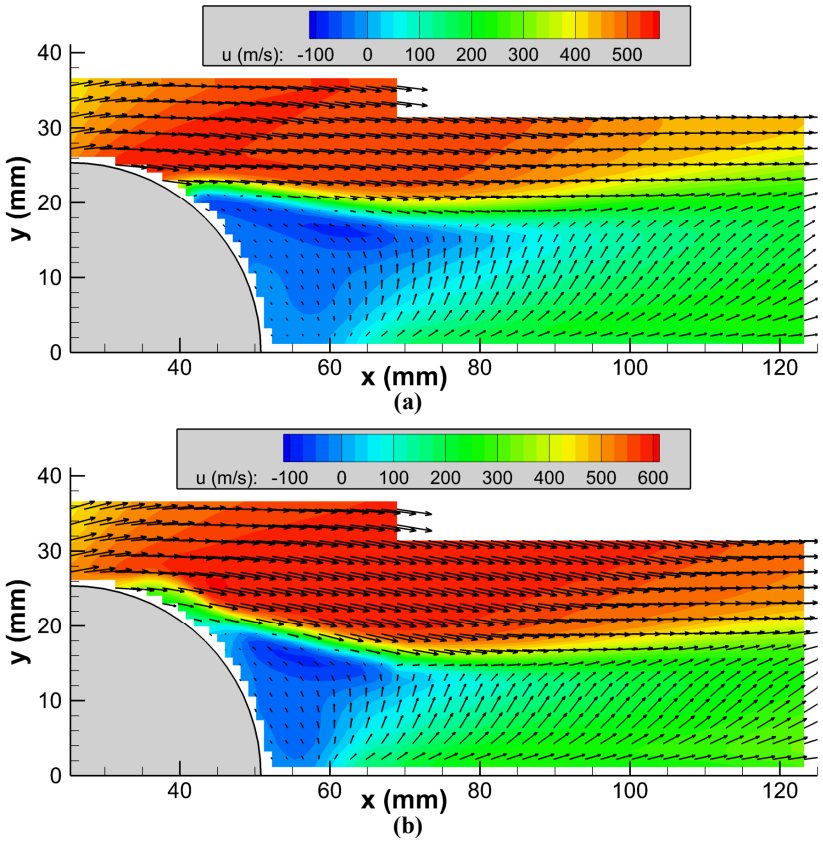

Fig. 4: Mean velocity field with in-plane vectors overlaid on a contour plot of the magnitude of the streamwise component. (a) Mach 1.5. (b) Mach 2.0. Vectors are subsampled 2 × 2 for clarity.

Figure 3 plots the mean streamwise velocity (Fig. 3a) and the streamwise turbulent normal stress (Fig. 3b) for each of these two subsamples along a profile through the wake at x=60 mm. Uncertainties were determined using Wieneke's method from correlation statistics [15] and propagated into turbulent stresses as per [16]. No significant difference is found between the two classes of seeding, indicating that the loss of vectors or entire bursts does not bias the measurements.

As a consequence of the tendency to lose adequate seed at Mach 2.0, fewer useful bursts were acquired as a percentage of total efforts. Original plans for data at Mach 2.5 were abandoned because adequate seeding of the wake was anticipated to be intractable.

Results and Discussion

Mean Velocity and Turbulent Stress Fields

Figure 4 shows the mean velocity field for the Mach 1.5 and Mach 2.0 cases. Vectors have been subsampled by a factor of two along each axis for visual clarity and are overlaid on a contour plot of the streamwise velocity magnitude. The mean flowfield shows a relatively small recirculation region immediately downstream of the hemisphere. This recirculation region and the wake height both diminish at Mach 2.0 in comparison to Mach 1.5. A recompression shock is present downstream of the recirculation region but is difficult to detect in the mean flow field because it is weak and unsteady and hence largely blurred out. Nonetheless, the presence of this shock is implied by the oblique contour lines and reduction of streamwise velocity magnitudes at the downstream end of the field of view. The lack of motion towards the wall, even within the recirculation region, suggests the possibility of mean three-dimensional motion where movement towards the wall occurs off the centerplane and the present data reveals only motion away from the wall.

The structure of the supersonic hemisphere wake differs considerably from that measured in a transonic flow. The PIV of Beresh et al [9] showed a much larger recirculation region with clear rotation within the streamwise plane of the measurement. In contrast, Fig. 4 shows motion moving away from the floor of the wind tunnel and outward

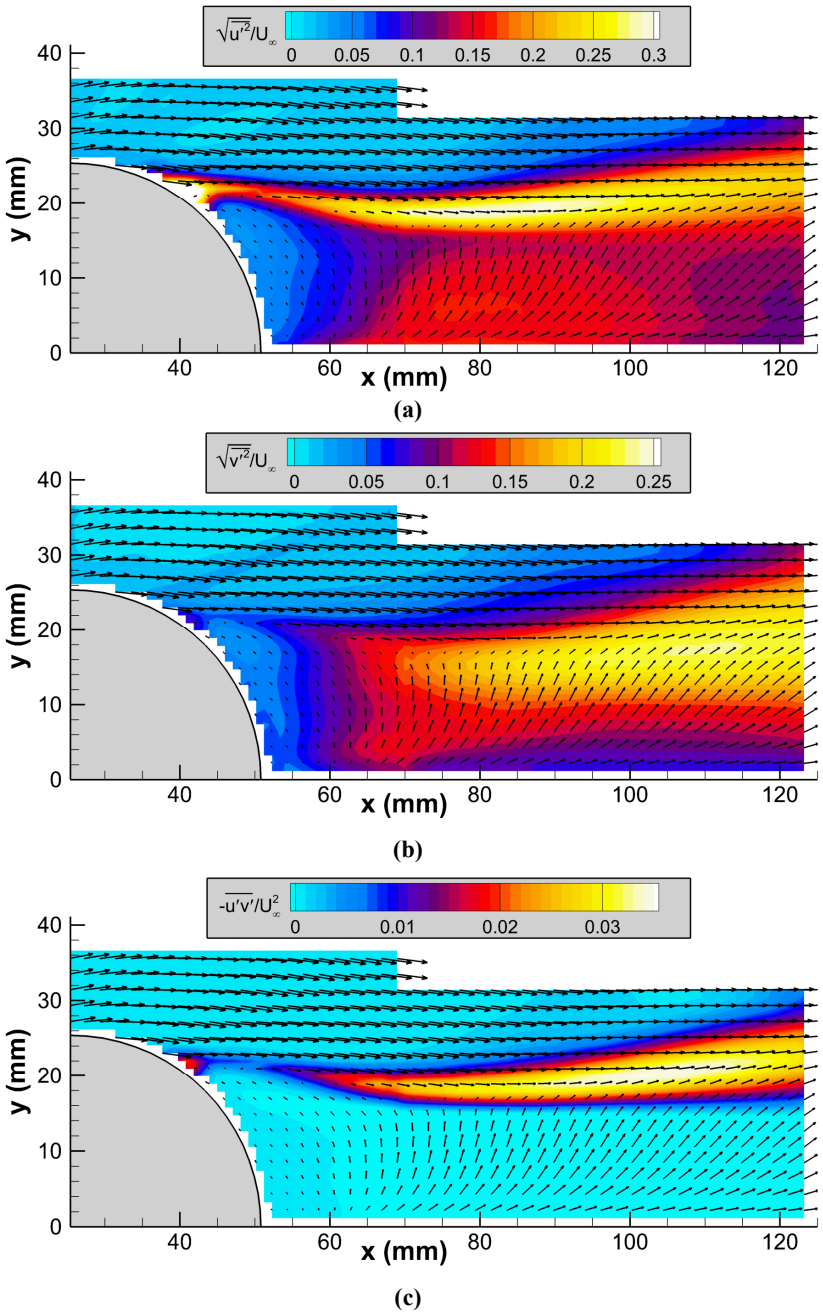

Fig. 5: Turbulent stress fields at Mach 1.5 with superposed mean vector field from Fig. 4. (a) streamwise normal stress; (b) vertical normal stress; (c) primary shear stress.

towards the freestream, with an upstream motion over the surface of the hemisphere and a downstream trajectory farther aft of the hemisphere. This is most plausible if the supersonic wake actually is formed of two lobes with a symmetry plane along the centerline. In this scenario, flow moves away from the wall near centerline, moves laterally, then returns to the wall off centerline. Morgan et al's simulations [11] also suggest that the supersonic wake of a hemisphere is split into two lobes with the possibility of flow moving outwards from the centerplane. A narrowing of the wake and change in gross structure for supersonic versus subsonic cases also was observed by Coirier et al [10].

Figures 5 and 6 show the three available turbulent stresses for the Mach 1.5 and 2.0 cases, respectively; these being the two normal stresses, u' and v', and the primary turbulent shear stress $u'v'$. Although pulse-burst PIV data are not ideal for measuring turbulent statistics because of the limited number of independent samples in time sequences of

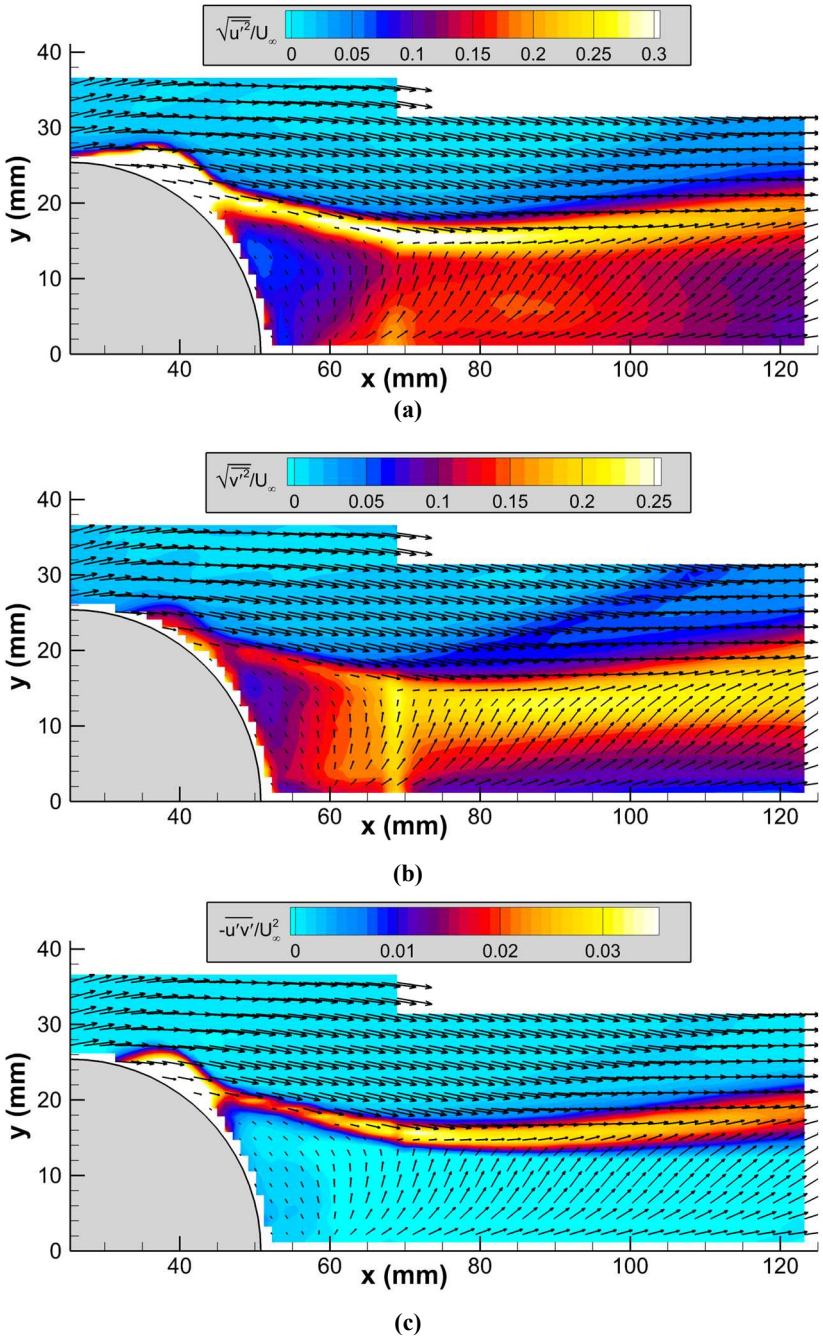

Fig. 6: Turbulent stress fields at Mach 2.0 with superposed mean vector field from Fig. 4. (a) streamwise normal stress; (b) vertical normal stress; (c) primary shear stress.

data, they are easily calculated from the present data though with greater uncertainty. Falchi and Romano [17] compared the convergence of mean and turbulence properties found from brief periods of TR-PIV data with that of low-speed PIV data acquired over a much longer duration and the effect on uncertainty. They found that the poorer statistical results from TR-PIV were readily explained by a smaller quantity of independent samples and the greater noise associated with high-speed cameras. Recently, Smith et al [18] have offered a procedure to determine the effective number of independent samples in time-resolved data to more accurately estimate convergence uncertainty. These experiences show that TR-PIV is suitable for statistically sampled quantities despite increased uncertainties,

though conventional PIV generally remains superior for such measurements. In the present case, turbulent data are well converged despite the small number of bursts because the integral time scales are much briefer than the burst duration (see subsequent analysis).

Despite these limitations in using the current data for turbulent statistics, the turbulent stress fields of Figs. 5 and 6 are enlightening, and have not previously been measured for such a flowfield. The shear layer that originates from the separation point on the hemisphere is clearly denoted by the u' and $u'v'$ fields; v' is broader and is more strongly activated a little downstream of the hemisphere once velocities have turned outward. The v' magnitudes reach a maximum at a different location than u', which indicates that not only is the flow anisotropic, but the anisotropy is varying spatially. Turbulent normal stresses are greatest in the shear layer but still significant within the wake; in contract, the turbulent shear stress is negligible within the wake. These plots indicate that the dominant activity behind the hemisphere is associated with the shear layer.

The presence of oblique shock waves can be weakly observed in the v' fields of Figs. 5b and 6b. At Mach 1.5, slightly elevated contours reveal a shock attached to the surface of the hemisphere just upstream of the separation point. Any shocks within the wake cannot be discerned here. Conversely, at Mach 2.0, an attached shock is not evident but an oblique shock can be seen emanating from the shear layer curvature farther downstream. The differing nature of the shock structure for the two Mach numbers will be explored subsequently.

Regardless of the difficulty seeding the near wake at Mach 2.0, there is no indication that the turbulent stresses have been artificially increased by greater noise or bias from undersampling. The general structure of the turbulent stress fields at Mach 2.0 is very similar to that at Mach 1.5, which is encouraging. Figure 3b additionally supports this contention. The maximum magnitudes of the turbulent stresses are modestly reduced at Mach 2.0 compared to Mach 1.5, which likely is a manifestation of the well-known effect in shear layers of increased compressibility inhibiting turbulent fluctuations (e.g., [19]). The blooming in intensity near the upper surface of the hemisphere evident in Figs. 6a and 6c is a result of laser flare interfering in the interrogation of PIV vectors. Too few valid bursts were available at Mach 2.0 to discard such occurrences as could be done at Mach 1.5.

Temporal Content

Figure 7 shows five sample sequential frames from one of the velocity sequences at Mach 1.5. Times are initial at the beginning of a burst of laser pulses and therefore arbitrary from a perspective of fluid dynamics. The size of the recirculation region is observed to vary during even this brief 100 μs period. The shear layer above it is fairly distinct and flaps significantly downstream of the recirculation region. Particularly interesting are the large-scale bulges in the shear layer extending into the freestream and the shocks attached to them. These bulges convect downstream between snapshots and the shocks move and deform with them. In the first vector field at t=3975 μs, a large bulge exits the field of view while another begins to form near x=90 mm. The second bulge grows as it convects downstream and a shock forms around it as its size protrudes into the freestream. By the final snapshot of the sequence at t=4075 μs, the bulge resembles the one that preceded it as it too exits the field of view. Another bulge is forming near x=80 mm with another shock emanating from it and propagating downstream from t=4050 μs to t=4075 μs. In all instances, the bulk motion within the wake remains away from the wall.

The PIV sequences may be studied quantitatively by performing cross-correlations on the temporal velocity signals across the entire field. Three different reference signals were used to assess the coherence of turbulent structures in particular regions of the flow. One reference signal was placed at in the center of the shear layer in its upstream region, just subsequent to separation. This corresponded to x=63 mm, y=19 mm for Mach 1.5 and x=63 mm, y=17 mm for Mach 2.0. A second location was chosen in the downstream region of the shear layer, at x=109 mm, y=22 mm for Mach 1.5 and x=109 mm, y=17 mm for Mach 2.0. Finally, the recirculation region was considered using a reference point at x=79 mm, y=7 mm for Mach 1.5 and x=83 mm, y=7 mm for Mach 2.0. Sequences of the resulting cross-correlation fields are given in Figs. 8, 9, and 10, for the three reference locations respectively. Correlations are shown for the streamwise velocity component, but results were similar for the vertical component, albeit that flow structures tend to exhibit turbulent structures whose long axes are roughly aligned to the vertical rather than the horizontal as for the streamwise component.

Figure 8 shows that a turbulent structure identified in the upstream shear layer correlates to an attached shock as it convects downstream. Every second time step is shown. This shock does not form immediately as the turbulent structure is shed from the hemisphere, but arises at time step t=50 μs at about x=70 mm for Mach 1.5 and x=80 mm for Mach 2.0 (though the attached shock is visible earlier for Mach 1.5). The angle of the shock appears to become more vertical as the structure convects downstream. The same behavior may be observed in Fig. 9 using the downstream reference location. In this case, the correlation strength is considerably more persistent, suggesting that coherent structures are better defined once the shear layer has grown somewhat. These turbulent structures are

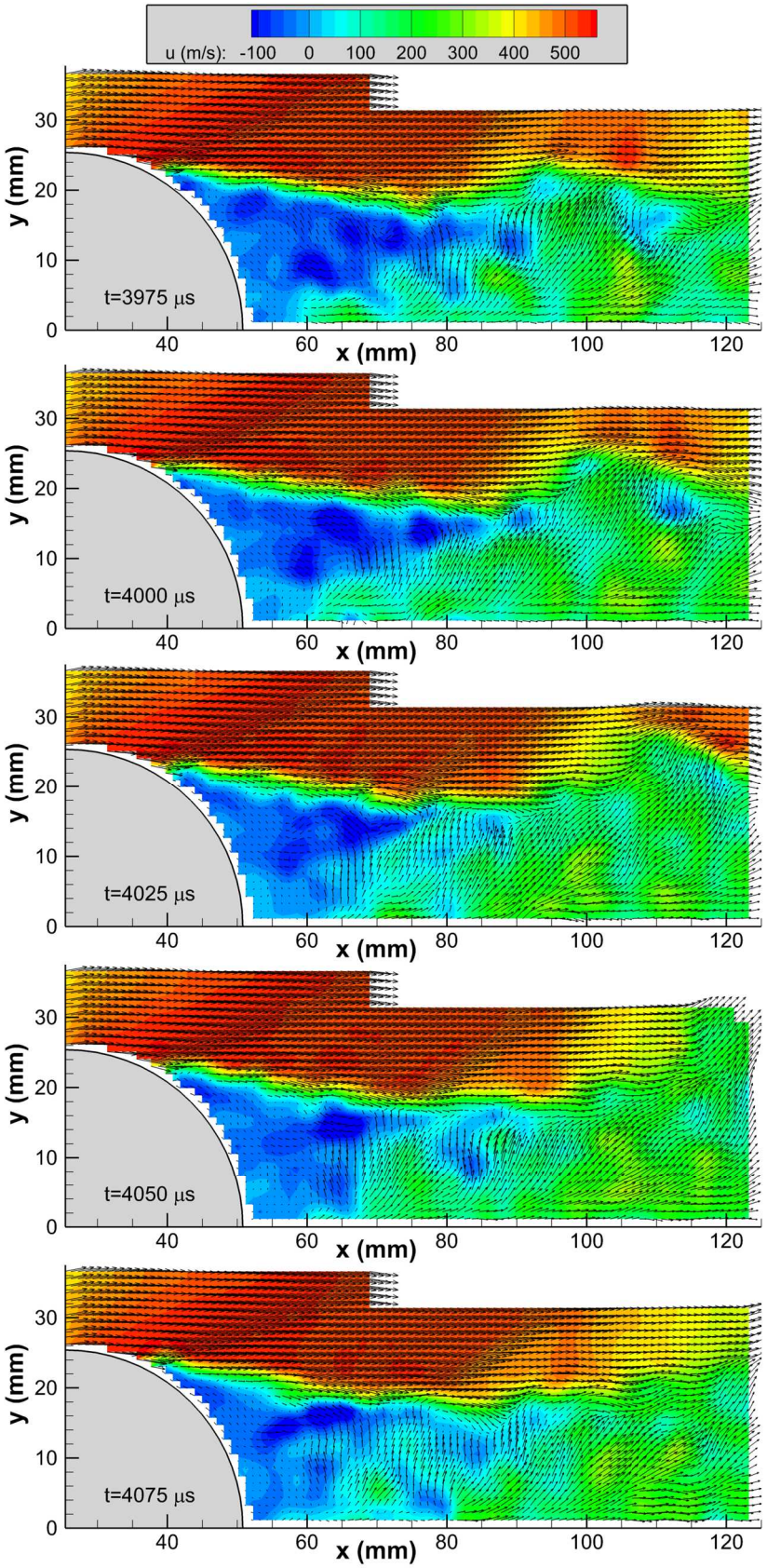

Fig. 7: Sequence of velocity fields at Mach 1.5 acquired at 40 kHz extracted from a burst 10.2 ms in duration composed of over 400 total frames. Initial time is arbitrary from the start of the burst.

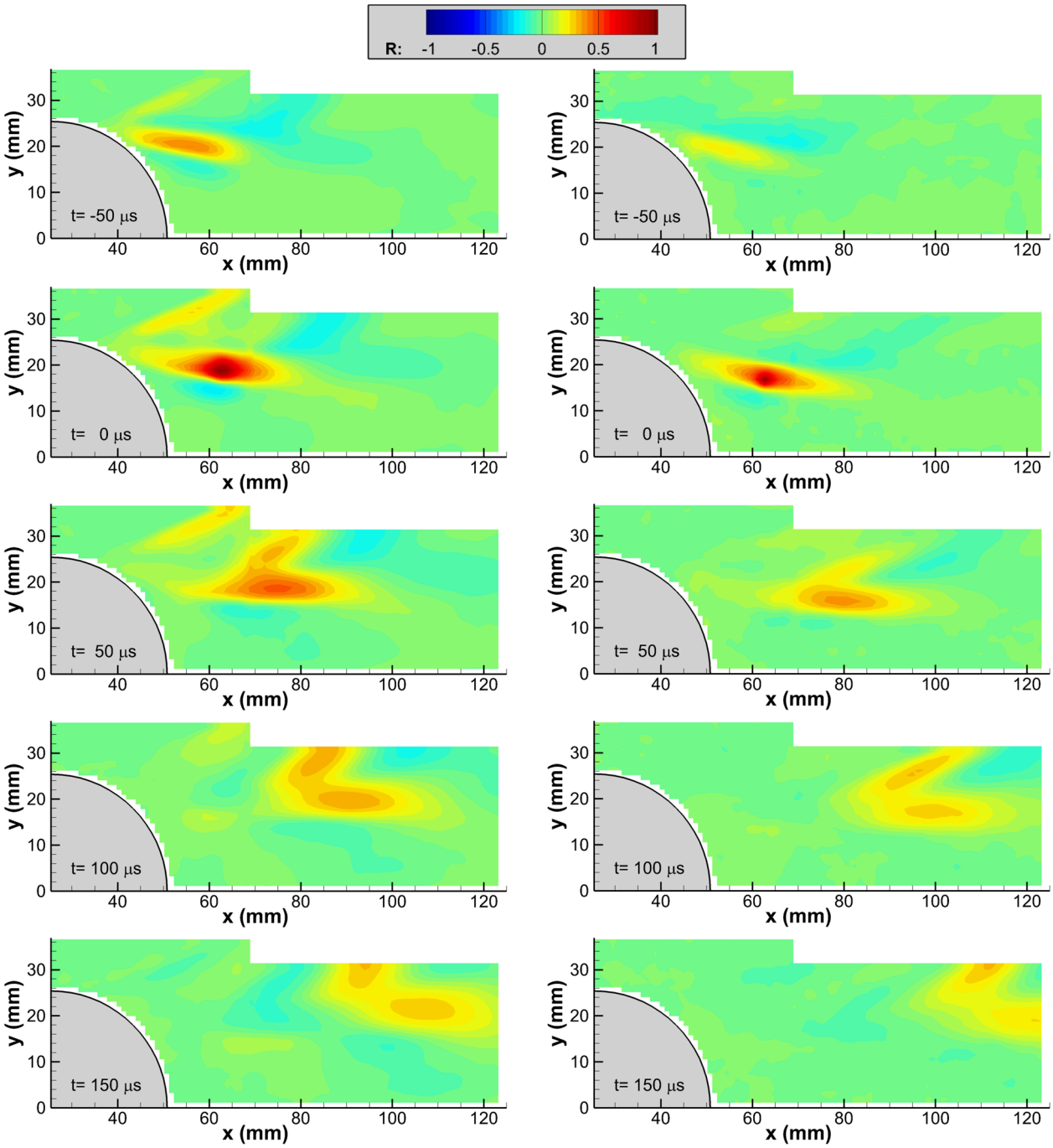

Fig. 8: Cross-correlation sequences of the streamwise velocity component to a reference location within the upstream center of the shear layer; (a) Mach 1.5 (x=63 mm, y=19 mm); (b) Mach 2.0 (x=63 mm, y=17 mm).

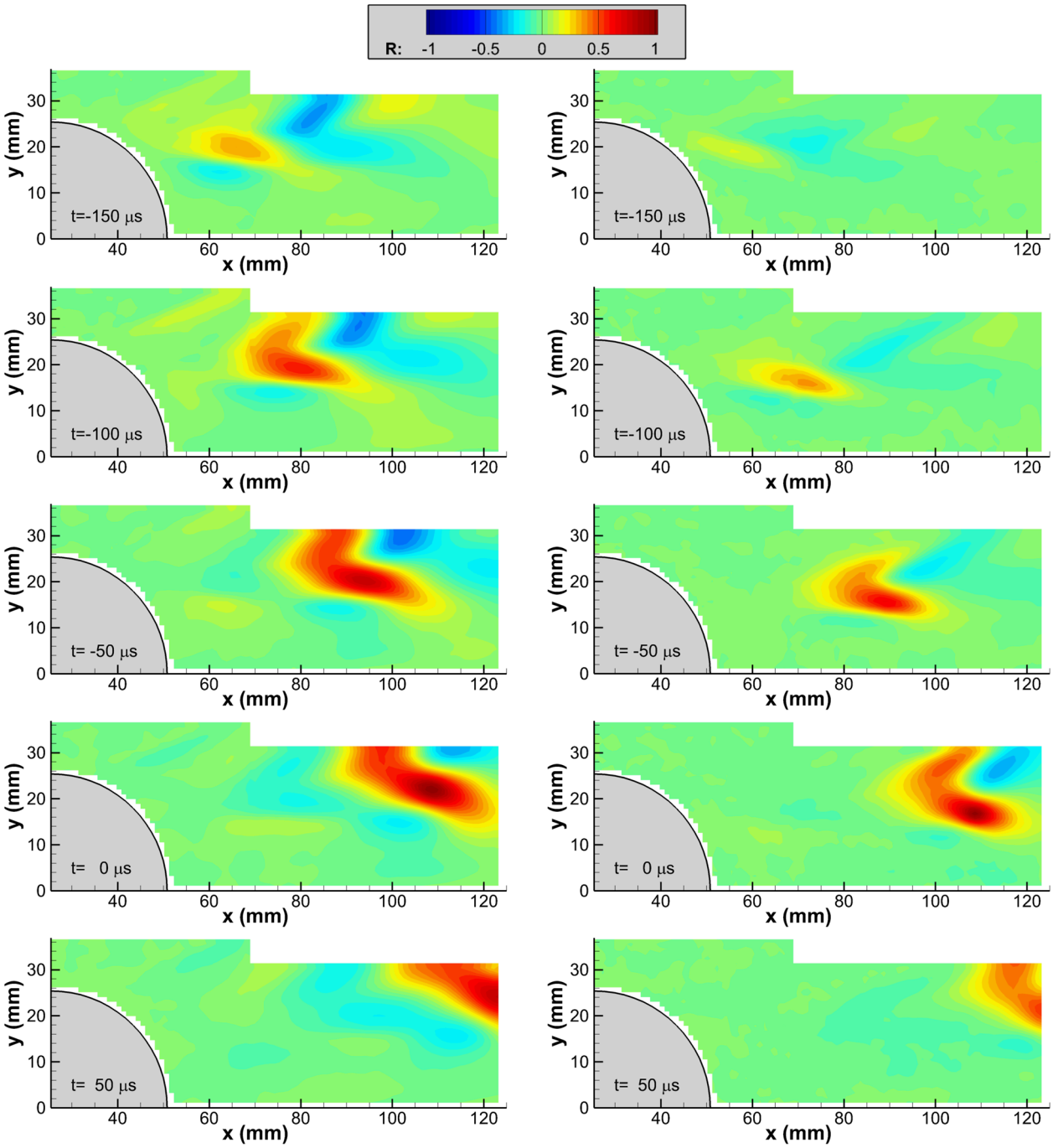

Fig. 9: Cross-correlation sequences of the streamwise velocity component to a reference location within the downstream center of the shear layer; (a) Mach 1.5 (x=109 mm, y=22 mm); (b) Mach 2.0 (x=109 mm, y=17 mm).

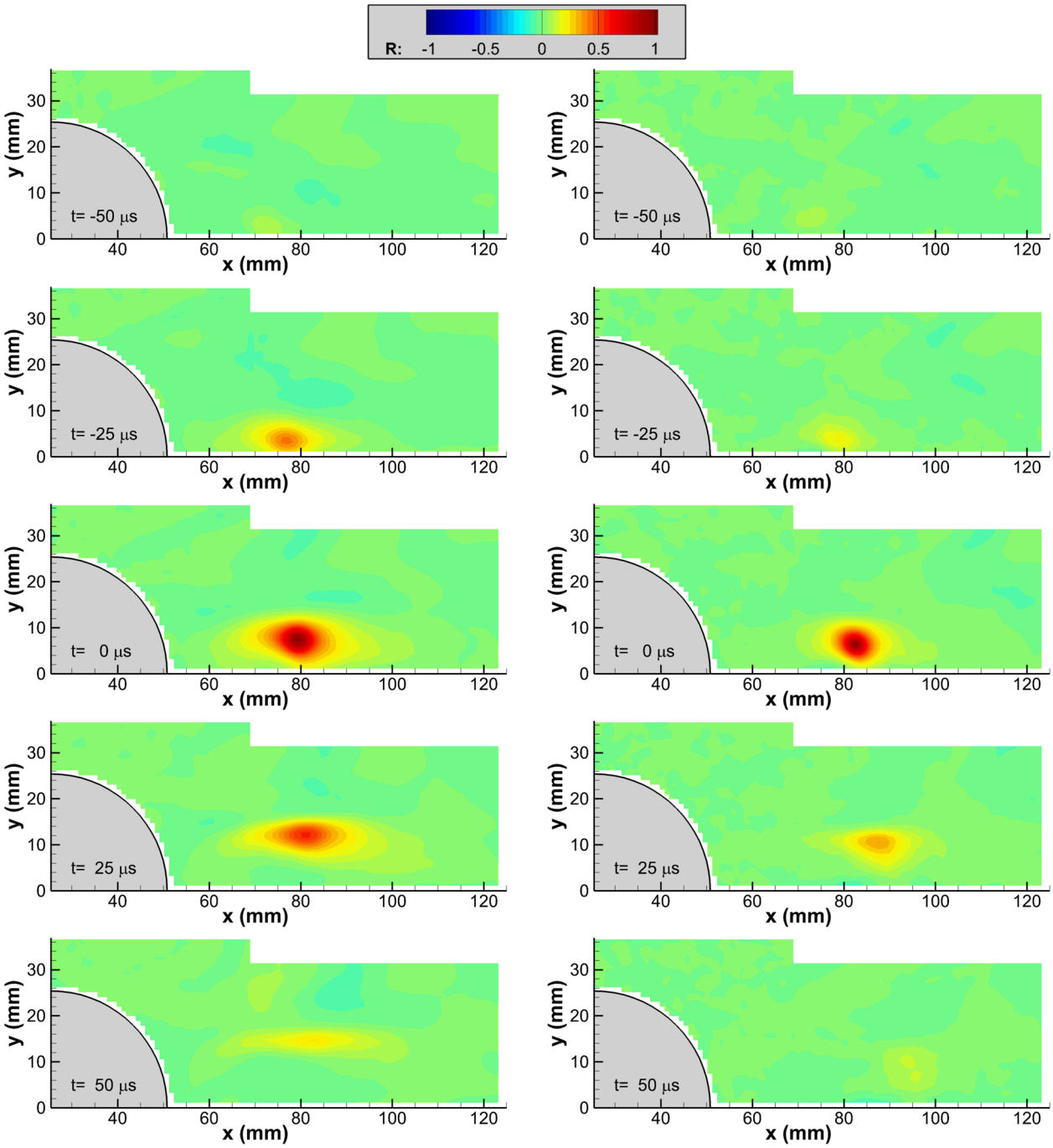

Fig. 10: Cross-correlation sequences of the streamwise velocity component to a reference location within the recirculation region; (a) Mach 1.5 (x=79 mm, y=7 mm); (b) Mach 2.0 (x=83 mm, y=6 mm).

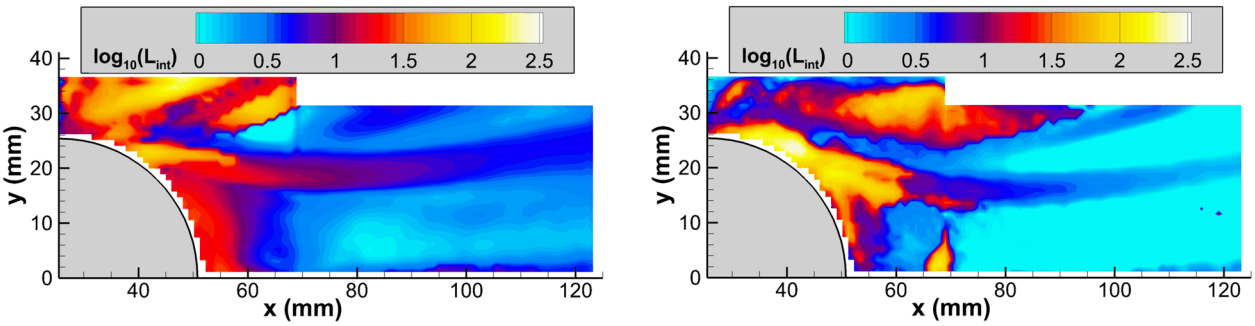

Fig. 11: Integral time constant (L_{int}) derived from auto-correlations of the streamwise velocity component, plotted in logarithmic form; units in microseconds; (a) Mach 1.5; (b) Mach 2.0.

noticeably smaller for Mach 2.0 than for Mach 1.5. Additionally, a stronger anti-correlation is visible above the turbulent structure and downstream of the shock, indicating a recovery of velocity subsequent to the shock.

Together, Figs. 8 and 9 clearly identify the convective motion of the oblique shock wave that forms in the wake of the hemisphere, which were only hinted by the mean and turbulent intensity plots of Figs. 4-6. The vague oblique shock seen in the mean velocity fields of Fig. 4 is the time average of many unsteady shocks such as observed in Fig. 7. Gordeyev and Jumper [1] conjectured that the oblique shock must be moving and indeed the cross-correlations show this to be the case. The oblique shock forms due to the development of a prominent bulge in the shear layer and then this oblique shock moves downstream as the turbulent bulge convects. The simulations of Coirier et al [10] also show this behavior when instantaneous snapshots of their unsteady flow are examined.

Cross-correlations in the recirculation region are shown in Fig.10, and the duration of the correlation is much briefer than those measured in the shear layer, requiring that successive time steps are shown rather than every second time step as in Figs. 8 and 9. The correlation strength diminishes more rapidly at Mach 2.0 than Mach 1.5, which may simply be a reflection of the briefer time scales associated with the greater flow velocity. No structures within the shear layer correlate with the recirculation region, indicating that turbulent structures within these two flow domains do not interact. A slight vertical rise in the coherent structure is seen, but no recirculating motion is evident. This would be consistent with the concept of a lobed separation region, in which recirculation occurs off the centerline of the flow.

A more efficient means of characterizing the persistence of turbulent structures in the flow is to calculate the integral time scale. This was accomplished by calculating the autocorrelation of each point in the velocity field, then integrating from t=0 until the first zero-crossing. The resulting integral time scale, L_{int}, is plotted in Fig. 11 for both Mach numbers using a logarithmic scale due to the wide range in resulting time scales. As for the cross-correlation results, the streamwise velocity component is shown but results using the vertical component are similar. Long time scales are found near the attached shock and in the very near wake of the hemisphere; in the Mach 2.0 case, this is complicated by the laser flare near the surface. Nonetheless, it is evident that once distant from the hemisphere surface, time scales are short in the shear layer and briefer still in the wake nearer the wall.

The brief time constants actually are helpful when considering the statistics of the pulse-burst data set. The typical time scale in the shear layer is no larger than about 20 μs, and considerably less farther downstream or in the recirculation region. Though a small number of bursts were acquired, the 10 ms burst duration is equivalent to 500 independent samples. Therefore, the statistical quality of the turbulence data in Figs. 5 and 6 is quite high despite having only 51 bursts at Mach 1.5 and 26 bursts at Mach 2.0.

These results differ from those implied by the cross-correlation fields, in which longer time durations are implied. For example, Fig. 9 shows correlations in the shear layer remaining considerably above zero for periods exceeding 200 μs, roughly an order of magnitude greater than those of the integral time constant. However, the auto-correlation upon which the integral time scale is based does not account for the convective motion of structures that is revealed by the cross-correlation sequences. When this is considered, the lifetime of turbulent structures appears considerably longer.

Frequency Spectra

Of course, one of the most powerful contributions of pulse-burst PIV is the ability to measure spectral content of the flow across an entire field of view. Velocity power spectral densities have been estimated at the same three

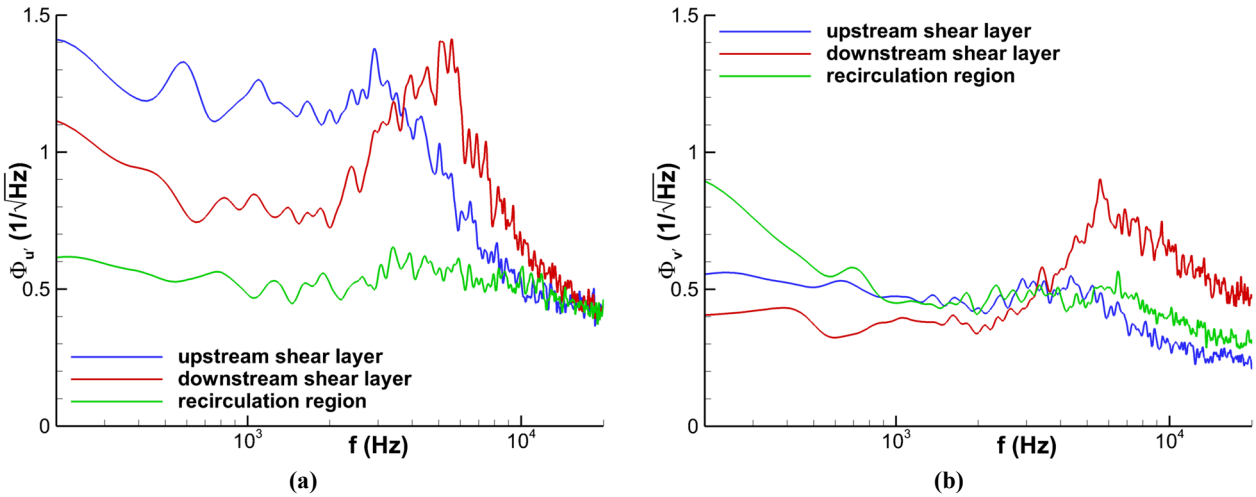

Fig. 12: Power spectral densities of the velocity fluctuations at Mach 1.5 at the three locations of the cross-correlations. (a) streamwise component; (b) vertical component.

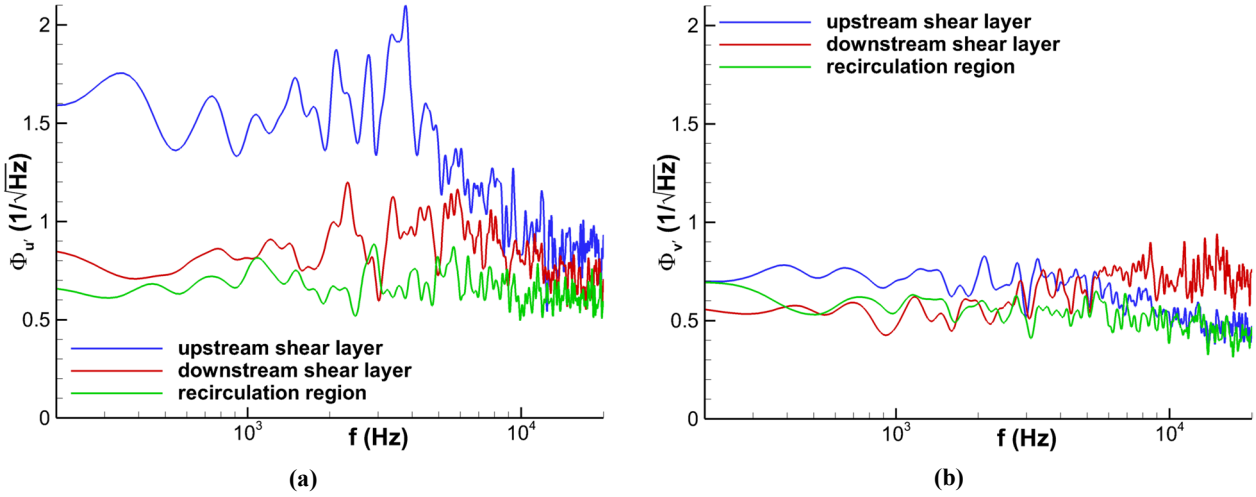

Fig. 13: As Fig. 12 but for Mach 2.0.

locations that were used for the cross-correlations: in the shear layer near the hemisphere, in the shear layer farther downstream, and within the recirculation region. Figure 12 shows the resulting spectra at Mach 1.5 for the streamwise and vertical components at these locations. Amplitudes of the vertical component are lower than the streamwise component, which is consistent with the smaller turbulent intensity of the vertical component seen in Fig. 5. The spectra in the upstream shear layer and the recirculation region are reasonably flat until they begin to roll off at higher frequencies but the spectra in the downstream shear layer exhibit a peak at about 5.6 kHz. This suggests that a preferred frequency exists as the shear layer flaps. It only becomes evident once the shear layer has grown downstream enough to have some range of motion.

The equivalent Mach 2.0 spectra are shown in Fig. 13 but are considerably noisier because they are generated from half as many bursts as the Mach 1.5 spectra. Nonetheless, it is apparent that no frequency peak emerges convincingly in the downstream shear layer. Spectra in the upstream shear layer and the recirculation region appear similar to their Mach 1.5 counterparts. Although this suggests that the shear layer does not flap at a preferred frequency for the Mach 2.0 case, analysis of the shock motion presented subsequently provides a fuller perspective on unsteady motion at both Mach numbers. This analysis indicates that in fact Mach 2.0 shock motion occurs at a preferred frequency of about 6.7 kHz, though not as distinctly as the Mach 1.5 shock motion.

Spectral information is available for every vector in the flow field, which allows the magnitude of the power spectral densities to be plotted spatially. Figure 14b shows the spatial distribution of the spectral magnitude at the preferred frequency of 5.6 kHz for the Mach 1.5 case. Conversely, Fig. 12 indicates that at a lower frequency of

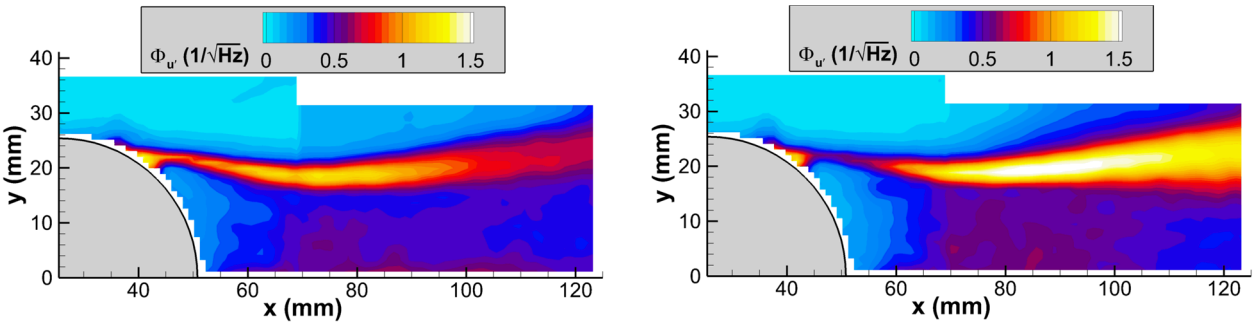

Fig. 14: Spatial distribution of the power spectral density amplitude of the streamwise velocity fluctuations at a specific frequency for 1.5. (a) f=2000 Hz; (b) f=5600 Hz.

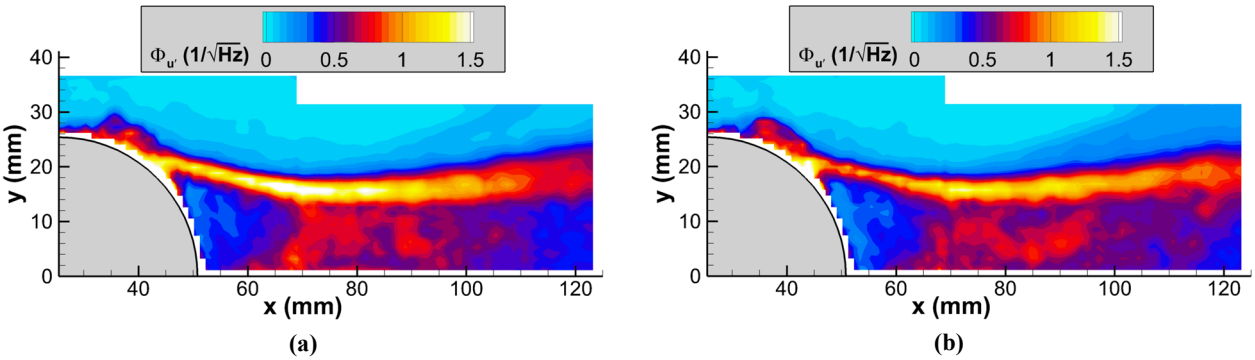

Fig. 15: As Fig. 14 but for Mach 2.0.

2 kHz, the spectra are relatively flat regardless of location and are representative of broadband turbulent motion; the spectral magnitude at this frequency is shown in Fig. 14a. A comparison of these two plots shows that the highest spectral magnitudes are concentrated in the shear layer regardless of frequency, which is where the highest levels of turbulence already have been found (Fig. 5). However, the elevated magnitudes display a greater width across the shear layer at 5.6 kHz than they do at 2 kHz, which could be attributed to a broader range of motion from the flapping of the shear layer at its preferred frequency.

Similar data are plotted in Fig. 15 for the Mach 2.0 case. Again, spectral magnitudes are tightly concentrated within the shear layer at both the turbulent frequency (2 kHz) and the preferred frequency (6.7 kHz). In this case, however, the spectral magnitudes do not possess a wider spatial footprint at the preferred frequency. This would be consistent with the preferred frequency becoming apparent only in the shock motion analysis that follows in the next section, not the shear layer velocity spectra of Fig. 13. Somewhat higher spectral magnitudes are found in the wake nearer the wall than compared with Mach 1.5, which again is consistent with the turbulence magnitudes reported in Fig. 6.

Shock Motion

The unsteady shocks emanating from the wake of the hemisphere are not readily visualized by velocity field sequences such as Fig. 7. Although the cross-correlations of Figs. 8 and 9 are able to extract the shock motion from the velocity data, such an analysis is representative of the entire data set and cannot provide instantaneous visualizations of the shock motion. Instead, shock positions are well identified by finding the divergence of the velocity field and plotting negative magnitudes, which denote compression. This is performed in Figs. 16 and 17 for Mach 1.5 and 2.0, respectively. Also shown is the instantaneous shear layer as identified by the vorticity, which is shown as the red flood contours, over which are superposed blue-white line contours of the divergence. However, divergence also is elevated by turbulent activity within the wake, so these plots only display the divergence beyond the shear layer as demarcated by the peak vorticity. The shocks appear to be thickened as a result of the finite particle lag, but are still well-defined in space.

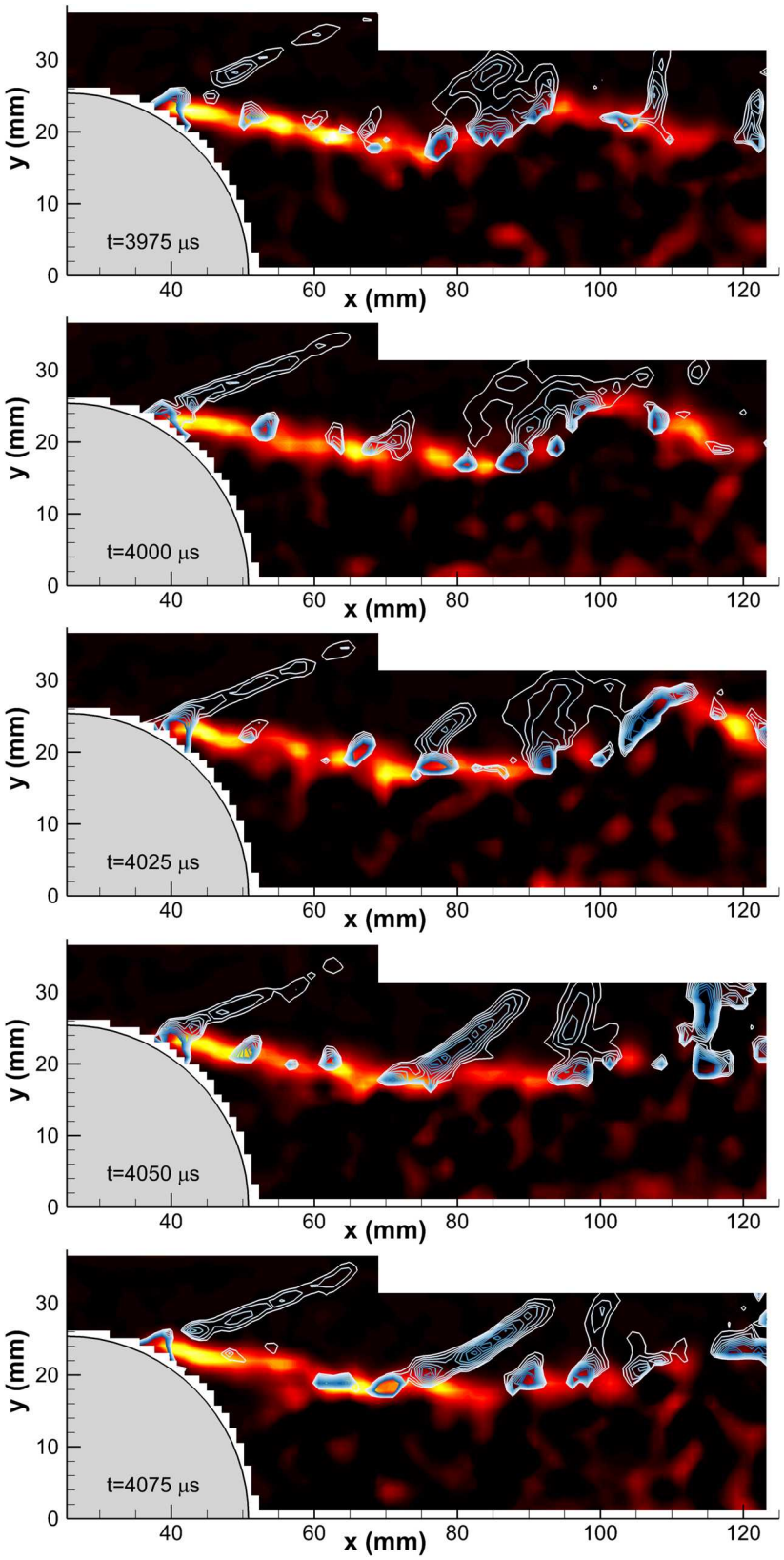

Fig. 16: The Mach 1.5 velocity field sequence of Fig. 7 post-processed to show the shear layer by the magnitude of the vorticity field (red flood contours) with superposed negative divergence contours plotted outside the shear layer to highlight shock waves (blue-white line contours).

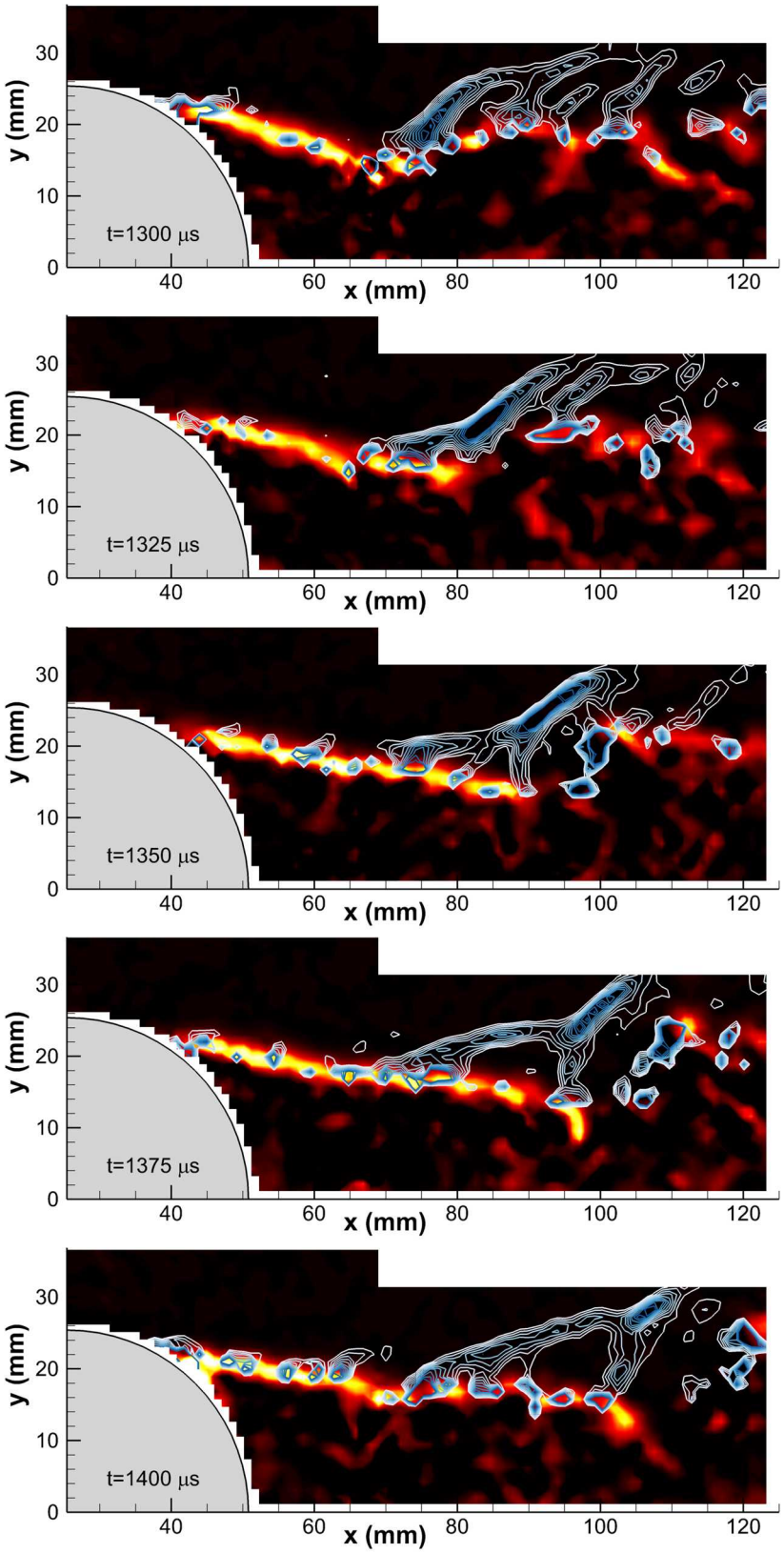

Fig. 17: As Fig. 16, but a sample Mach 2.0 velocity field sequence.

Figure 16 shows the divergence and vorticity for the same velocity fields as provided in Fig. 7. The turbulent bulge identified in Fig. 7 as it convects beyond the field of view is evident in the undulations of the vorticity field. Vorticity appears stronger on the leading edge of this bulge, with its trailing edge dominated by a rise in divergence magnitude that marks the shock wave affixed to the turbulent structure. This shock is first observed at t=3975 µs and x=80-90 mm where it is just beginning to coalesce as the shear layer flaps upwards and forms a bulge. As this bulge grows and convects, the shock becomes more distinct, appearing better ordered at t=4025 µs, then evolving into a more upright position in the subsequent time step. Meanwhile, another oblique shock forms behind it beginning at about t=4025 µs and then growing and sharpening from there. A weaker disturbance appears to be present between them. Shocks propagating downstream do not display any interaction between them.

Shock motion at Mach 2.0 is somewhat different, as observed in Fig. 17. Here, several smaller disturbances appear to coalesce a short distance above the shear layer, with the angle of these shocks changing as this occurs. In the first time step, t=1300 µs, several disturbances between x=70 and x=100 mm are beginning to become linked as they propagate from the shear layer. At t=1350 µs, one stronger oblique shock has formed with bifurcated feet at three locations. One time step later this has settled into two shock feet. The coalesced portion of the shock can be observed to convect downstream with the shear layer but the shock feet demonstrate variant motion as they coalesce and break apart. The downstream-most shock foot in the frames from t=1350 to 1400 µs also convects with shear layer structures. Playing out the sequence further (not shown) suggests that the coalesced oblique shock begins to break up rather than exit the field of view, then reforms from new shock feet associated with subsequent turbulent shear layer structures. This bifurcated behavior is characteristic of the entire data set and is visually dissimilar from the Mach 1.5 data set.

The frequencies of shock motion may be determined by finding the power spectra of the divergence field to compare with those of the velocity field shown previously in Figs. 12 and 13. The most common shock location can be found by computing the mean of the divergence field (not shown for brevity), then picking out the peak divergence location near the edge of the field of view. For Mach 1.5, this reveals a most probable shock location of x=90 mm, y=29 mm, and for Mach 2.0, it is x=101 mm, y=29 mm. Figure 18 shows the power spectra at these locations. The Mach 1.5 spectrum looks much like the spectra of the velocity field shown in Fig. 12, complete with a prominent peak at 5.6 kHz as the downstream shear layer showed. This confirms that the shock motion and shear layer flapping exhibit similar properties once allowed to grow from their origin. On the other hand, the spectra of the Mach 2.0 velocity field found in Fig. 13 did not show a prominent frequency peak, but the spectrum in Fig. 18 of the divergence field reveals a weak peak near approximately 6.7 kHz. This suggests that there is an ordered component to the Mach 2.0 shock motion even if it is not as well coupled to repeatable motion of the shear layer. Though the greater noise due to fewer bursts at Mach 2.0 as compared with Mach 1.5 makes the peak more difficult to discern, it nevertheless appears that the preferred frequency of shock motion is weaker at the higher Mach number.

The typical behavior of the shock motion and its coupling to the shear layer unsteadiness can be determined using conditional ensemble averages. The most probable shock locations used to find the spectra of Fig. 18 also are used as trigger locations for creating an ensemble. When the divergence magnitude exceeds a threshold of approximately 1/3

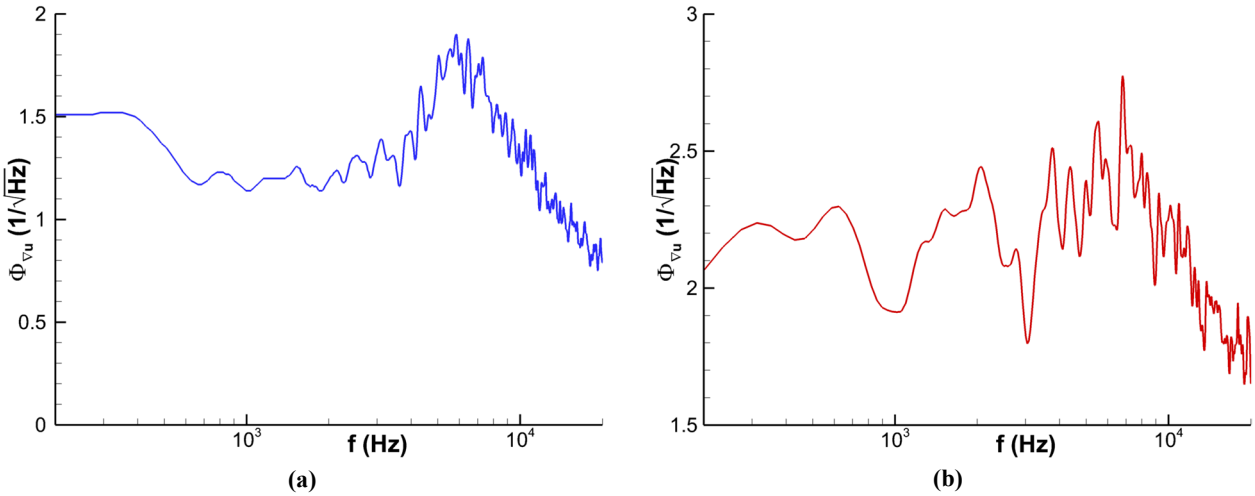

Fig. 18: Power spectral densities of the divergence of velocity where the shock motion is strongest. Magnitudes multiplied by 10^4. (a) Mach 1.5 (x=90 mm, y=29 mm); (b) Mach 2.0 (x=101 mm, y=29 mm).

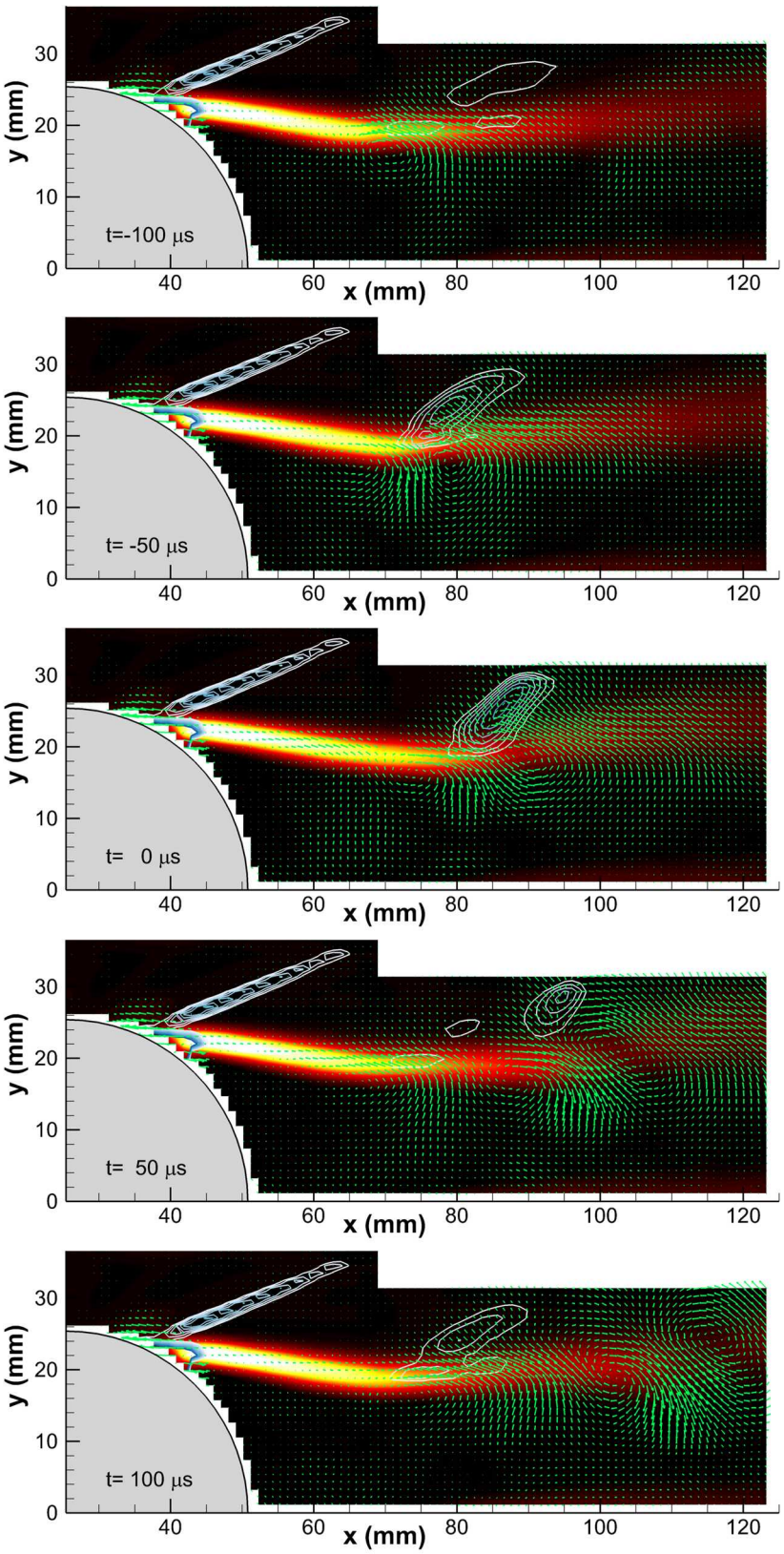

Fig. 19: Conditional velocity field sequences at Mach 1.5. The shear layer is shown by the magnitude of the vorticity field (red flood contours), the shock waves by negative divergence contours (blue-white line contours), and conditionally-averaged vortices by the velocity field (green vectors). Note that every second time step is shown.

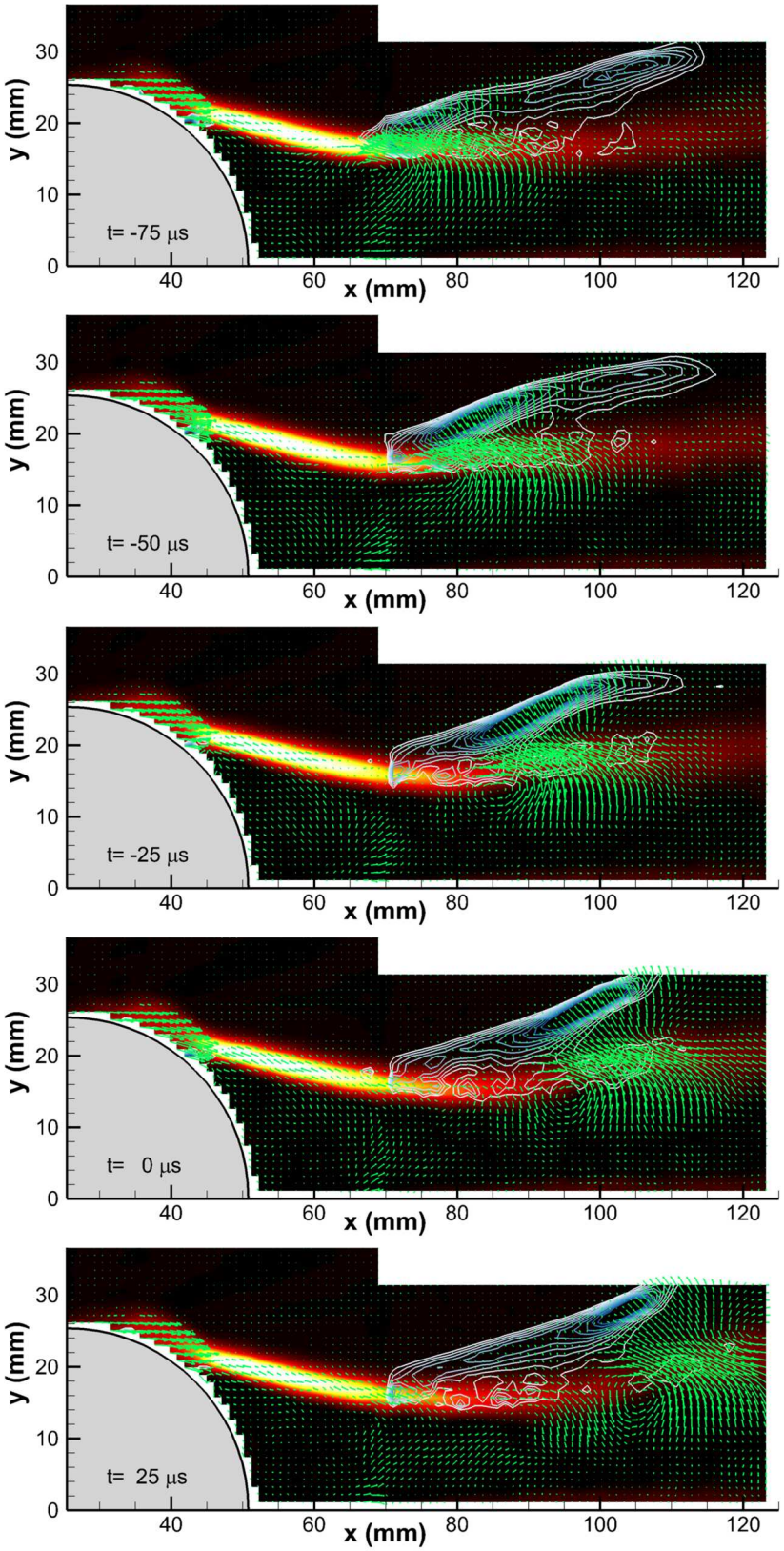

Fig. 20: As Fig. 19 but for Mach 2.0. Each time step is shown.

its maximum value, the vector field and derived vorticity and divergence fields are added to the ensemble, as are a few time steps before and after the trigger event. This yields a conditional time sequence that shows the characteristic evolution of all aspects of the hemisphere wake.

Figure 19 shows the ensemble-averaged time sequence for the Mach 1.5 case. This includes the vorticity field to identify the shear layer and the divergence field beyond the shear layer to mark the shock positions, as in Figs. 16 and 17, but now additionally shows velocity vectors of turbulent structures in the shear layer linked to the conditional trigger event. The trigger event is shown as t=0, plus two time steps before and after this event; every second time step is shown to capture the time period over which repeatable motion occurs.

Two primary discoveries emerge from Fig. 19. First, a counter-rotating vortex pair is evident in the vector field associated with the unsteady shock position. The shock originates approximately at the midpoint between the two vortices. The shock and vortex pair propagate downstream in tandem. A ripple in the vorticity pattern is found to propagate downstream with the vortex pair as well, where the bend in the shear layer corresponds to the midpoint between the two vortices and the shock foot. At the t=50 μs and t=100 μs time steps, two such ripples may be found since a third vortex becomes apparent. Secondly, the unsteady shock motion displays periodicity. The shock associated with the trigger event at t=0 can be seen to originate at t=-100 μs at approximately x=70 mm, or perhaps more clearly at t=-50 μs and x=75 mm. As this shock has dissipated farther downstream by t=100 μs, another shock is seen to form at x=75 mm. If the shock is considered to originate between t=-100 and -50 μs (confirmed by the full movie sequence), this corresponds to a shock period of 175 μs, which is a frequency of 5.7 kHz. This well matches the preferred frequency of motion of 5.6 kHz extracted from the spectra of Figs. 12 and 18. No relation is found between the unsteady shock and the shock affixed to the hemisphere surface.

The ensemble-averaged time sequence for Mach 2.0 is given in Fig. 20. The rippling of the oblique shock occurs on shorter time scales than the shock period of the Mach 1.5 case, so here successive time steps are shown from t=-75 μs to t=25 μs. The evidence for bifurcated shock feet is weak, limited to a spatial spreading at the base of the shock, although a weak forward shock foot may be distinguishing itself from the primary shock at the t=-25 μs time step. Unlike Mach 1.5, propagation of the shock wave does not appear to occur; instead, the shock ripples and deforms as the vortex pair passes through it. However, the cross-correlations of Figs. 8 and 9 did indicate a traveling shock wave associated with the convecting turbulent structure, which also is apparent in the instantaneous sequence of Fig. 17. This apparent discrepancy may occur because the bifurcated shock feet behave differently than the coalesced oblique shock and respond differently depending upon the conditional trigger. The ensemble-average trigger follows the representative oblique shock motion tied to the preferred frequency of 6.7 kHz, which reveals that the coalesced shock ripples as shear layer vortices pass rather than convecting towards the exit of the field of view. Conversely, the cross-correlations are conditioned on shear layer behavior and therefore find an association between shock foot motion and coherent shear layer structures that does not possess any periodicity. That is, the shock foot tends to move with a shear layer structure but does not recur at a preferred frequency. The coalesced shock ripples at a preferred frequency that is detected when the shock is used as a conditional trigger in the ensemble averages but not when the shear layer is used as a reference in the cross-correlations.

The vector field of Fig. 20 suggests that the upwash between the two vortices is responsible for the rippling of the shock, and that the correlation is stronger with the downstream-most vortex in the pair, which rotates with positive sign. In contrast, at Mach 1.5 it was downwash between the vortices that correlated most strongly with the shock position, with the positive vortex leading the pair. The sequence of Fig. 20 is not long enough to establish periodic behavior, which would be expected over 150 μs, but the full movie sequence reveals that a single ripple of the shock occurs during this time frame.

Conclusions

A pulse-burst laser was used to obtain time-resolved particle image velocimetry (PIV) measurements of the supersonic flow over a wall-mounted hemisphere. Data were acquired at 40 kHz in the wake of the hemisphere within the streamwise plane along the centerline at Mach 1.5 and 2.0. Mean velocity and turbulent stress fields are presented, which are well converged despite the low duty cycle of pulse-burst PIV because the integral time scales are much briefer than the burst duration. The recirculation region and wake height are reduced at Mach 2.0 as compared to Mach 1.5. A lack of motion towards the wall suggests a recirculation region with two lobes in which flow moves away from the wall near centerline and recirculates back towards the hemisphere off centerline, in contrast to a more conventional recirculation region found in the subsonic compressible regime.

Through the use of spatio-temporal cross-correlations and conditional ensemble averages, the characteristic behavior of the unsteady shock motion is captured and related to the flapping of the shear layer. At Mach 1.5, oblique shocks are associated with vortical structures in the shear layer and form a short distance downstream of the

hemisphere rather than immediately as the turbulent structure is shed from the hemisphere surface. Shocks propagate downstream without apparent interaction between them, consistently positioned between counter-rotating shear layer vortices. A weak periodicity is observed in both the flapping of the shear layer and the formation of oblique shocks.

Shock motion at Mach 2.0 is somewhat different, wherein multiple weak disturbances propagate from the shear layer and coalesce to form an oblique shock farther out. The coalesced portion of the shock can be observed to ripple as shear layer structures pass by. Meanwhile, the bifurcated shock feet convect downstream attached to turbulent structures in the shear layer, coalescing and breaking apart without apparent repeatability as they do.

Power spectra show a preferred frequency of shear layer flapping and shock motion at 5.6 kHz for Mach 1.5, but at Mach 2.0 a weak preferred frequency of 6.7 kHz is found only for the oblique shock motion and not the shear layer unsteadiness.

References

[1] Gordeyev, S., and Jumper, E., "Fluid Dynamics and Aero-Optics of Turrets," *Progress in Aerospace Sciences*, Vol. 46, No. 8, 2010, pp. 388-400.

[2] Reid, J. Z., Lynch, K. P., and Thurow, B. S., "Density Measurements of a Turbulent Wake Using Acetone Planar Laser Induced Fluorescence," *AIAA Journal*, Vol. 51, No. 4, 2013, pp. 829-839.

[3] Fang, S., Disotell, K. J., Long, S. R., Gregory, J. W., Semmelmeyer, F. C., and Guyton, R. W., "Application of Fast-Responding Pressure-Sensitive Paint to a Hemispherical Dome in Unsteady Transonic Flow," *Experiments in Fluids*, Vol. 50, No. 6, pp. 1495-1505, 2011.

[4] Morrida, J., Gordeyev, S., Jumper, E., Gogineni, S., and Wittich, D. J., "Investigation of Shock Dynamics on a Hemisphere Using Pressure and Optical Measurements," AIAA Paper 2016-1348, January 2016.

[5] Morrida, J., Gordeyev, S., and Jumper, E., "Transonic Flow Dynamics Over a Hemisphere in Flight," AIAA Paper 2016-1349, January 2016.

[6] Morrida, J., Gordeyev, S., De Lucca, N., and Jumper, E., "Aero-Optical Investigation of Transonic Flow Features and Shock Dynamics on Hemisphere-on-Cylinder Turrets," AIAA Paper 2015-0676, January 2015.

[7] Goorskey, D. J., Drye, R., and Whiteley, M. R., "Dynamic Modal Analysis of Transonic Airborne Aero-Optics Laboratory Conformal Window Flight-Test Aero-Optics," *Optical Engineering*, Vol. 52, No. 7, 2013, pp. 071414.

[8] De Lucca, N., Gordeyev, S., and Jumper, E., "In-Flight Aero-Optics of Turrets," *Optical Engineering*, Vol. 52, No. 7, 2013, pp. 071405.

[9] Beresh, S. J., Henfling, J. F., Spillers, R. W., and Pruett, B. O. M., "Unsteady Shock Motion in a Transonic Flow over a Wall-Mounted Hemisphere," *AIAA Journal*, Vol. 54, No. 11, 2016, pp. 3509-3515.

[10] Coirier, W., Porter, C., Barber, J., Stutts. J., Whiteley, M., Goorskey, D., and Drye, R. "Aero-Optical Evaluation of Notional Turrets in Subsonic, Transonic and Supersonic Regimes," AIAA Paper 2014-2355, June 2014.

[11] Morgan, P. E., Sherer, S. E., and Visbal, M. R., "Numerical Exploration of Supersonic Flow over a Wall-Mounted Hemisphere," AIAA Paper 2016-3650, June 2016.

[12] Beresh, S. J., Kearney, S. P., Wagner, J. L., Guildenbecher, D. R., Henfling, J. F., Spillers, R. W., Pruett, B. O. M., Jiang, N., Slipchenko, M., Mance, J., and Roy, S., "Pulse-Burst PIV in a High-Speed Wind Tunnel," *Measurement Science and Technology*, Vol. 26, No. 9, 2015, pp. 095305.

[13] Samimy, M., and Lele, S. K., "Motion of Particles with Inertia in a Compressible Free Shear Layer," *Physics of Fluids A*, Vol. 3, No. 8, 1991, pp. 1915-1923.

[14] Melling, A., "Tracer Particles and Seeding for Particle Image Velocimetry," *Measurement Science and Technology*, Vol. 8, No. 12, 1997, pp. 1406-1416.

[15] Wieneke, B., "PIV Uncertainty Quantification from Correlation Statistics," *Measurement Science and Technology*, Vol. 26, No. 7, 2015, pp. 074002.

[16] Sciacchitano, A., and Wieneke, B., "PIV Uncertainty Propagation," *Measurement Science and Technology*, Vol. 27, No. 8, 2016, pp. 084006.

[17] Falchi, M., and Romano, G. P., "Evaluation of the Performance of High-Speed PIV Compared to Standard PIV in a Turbulent Jet," *Experiments in Fluids*, Vol. 47, No. 3, 2009, pp. 509-526.

[18] Smith, B. L., Neal, D. R., and Feero, M., "Re-thinking of Data Acquisition Rates in the Era of Expensive Data," submitted to *Measurement Science and Technology*, 2016.

[19] Smits, A. J., and Dussauge, J.-P., *Turbulent Shear Layers in Supersonic Flow*, 2nd ed., Springer, New York, 2006, pp. 139-178.